



RESEARCH ARTICLE

Gold Nanorods Coated with Palladium-Platinum Alloy Shell Superstructures for Enhanced Plasmon-Driven Photocatalysis

Zhen-Ming Shen¹  | Jie Liu¹ | Qi Zhang¹ | Er-Ji Zhang¹ | Xiaoyu Zhao² | Yiqiang Gao¹ | Zhigang Zhou¹ | Tian-Song Deng¹ 

¹School of Electronics and Information Engineering, Hangzhou Dianzi University, Hangzhou, P. R. China | ²College of Materials and Environmental Engineering, Hangzhou Dianzi University, Hangzhou, P. R. China

Correspondence: Jie Liu (liujie4209@hdu.edu.cn) | Yiqiang Gao (yqgao@hdu.edu.cn) | Tian-Song Deng (dengts@pku.edu.cn)

Received: 1 July 2025 | **Revised:** 28 September 2025 | **Accepted:** 6 October 2025

Keywords: gold nanorods | localized surface plasmon resonance | photocatalysis | plasmon-driven | superstructures

ABSTRACT

Bimetallic and trimetallic nanostructures offer unique physicochemical properties for enhancing photocatalytic performance. In this work, a facile and reproducible method of preparing palladium-platinum (PdPt) alloy shell on gold nanorods (AuNRs) is designed for enhancing the catalytic reactions under light irradiation. Specifically, Pd and Pt shells are sequentially deposited on the surface of AuNRs, forming well-defined core-shell Au@PdPt superstructures (Au@PdPt SSs). Photocatalytic activity is evaluated through the NaBH₄-mediated reduction of methyl blue (MB), demonstrating that Au@PdPt SSs exhibit significantly enhanced photocatalytic performance under light irradiation compared to bimetallic counterparts or single-component analogs. Finite-difference time-domain simulations reveal that the spatial distribution of the enhanced electric field closely correlates with the structural characteristics of the Au@PdPt SSs, confirming the influence of morphology on plasmonic behavior. The localized surface plasmon resonance (LSPR) of Au promotes hot electron generation and transfer to the catalytic PdPt alloy shell surface. The results highlight the synergistic interaction between plasmonic Au core and catalytic PdPt shells, where plasmon-induced charge separation and migration play a pivotal role. This work provides a rational design strategy for constructing high-efficiency plasmon-mediated photocatalysts based on multi-metallic nanostructures, with potential applications in green chemistry and environmental remediation.

1 | Introduction

Noble metal nanostructures exhibit unique properties that differ from those of their bulk counterparts. In particular, nanostructures made of gold and silver demonstrate excellent performance in light absorption and scattering [1–10]. When light is incident on noble metal nanoparticles, and the frequency of the incident photons matches the collective oscillation frequency of the conduction electrons in the nanostructure, the nanoparticles strongly absorb the photon energy, resulting in

a pronounced resonance absorption peak in the spectrum. This phenomenon is known as LSPR [5, 11, 12]. Due to this unique effect, noble metal nanostructures have attracted extensive attention in both scientific research and technological applications.

Over the past two decades, researchers have made significant efforts in designing and synthesizing noble metal nanostructures of various morphologies. AuNRs, in particular, have shown great application potential in surface-enhanced Raman scattering

(SERS) sensors [13–17], solar cells [18–20], biomedicine [5, 21–25], and catalysis [26–34], owing to their shape-dependent LSPR characteristics.

In recent years, researchers have moved beyond the exploration of single-metal nanostructures and have begun to investigate the growth of other metals on the surfaces of noble metal nanostructures to obtain bimetallic or even trimetallic nanostructures, which has been extensively studied [35–39]. Generally, bimetallic nanostructures tend to combine the advantageous properties of both constituent metals. They can retain the LSPR features of plasmonic nanoparticles, like AuNRs, while gaining additional physicochemical properties—such as the catalytic activity of Pd and Pt [40–43]. For example, Yong et al. [37] used Au@Pd nanocrystals as a model system to systematically investigate the influence of Au core size/shape and Pd shell thickness on catalytic efficiency. The results showed that, under the same Pd loading, thinner shells and smaller core sizes facilitated higher reaction rates, with the nanorod structure exhibiting the highest catalytic efficiency and the strongest plasmonic enhancement effect. Gu et al. [38] successfully constructed a core-cage structured Au@AgPt trimetallic nanoframe catalyst, in which the embedded AuNRs serve as the plasmon-enhanced photothermal core for the reduction of 4-nitrophenol. This structure combines LSPR-induced local heating with catalytic active sites from the alloy, achieving excellent photothermal catalytic performance. The optimized Au@AgPt nanocatalyst completed the reduction reaction in approximately one minute. Zhuo et al. [39] successfully synthesized wavy Au@PdAu core-shell nanoplates via a seeded growth method, featuring tunable shell thickness and strong NIR absorption. These nanostructures exhibited excellent catalytic activity for 4-nitrophenol reduction under visible light, with a rate constant 6.76 times higher than that in the dark, highlighting a significant plasmonic-enhancement effect.

In this study, a simple and reproducible method was developed to fabricate a PdPt alloy shell on AuNRs for enhanced photocatalytic reactions. Specifically, using AuNRs as seeds, Pd²⁺ and Pt²⁺ precursors were sequentially added under different surfactant environments to form PdPt alloy shells on the AuNRs surfaces, yielding Au@PdPt SSs with various morphologies. Using MB as the reactant and Au@PdPt SSs as the catalyst, photocatalytic experiments were conducted. The results showed that Au@PdPt SSs synthesized using CTAB exhibited excellent photocatalytic performances. FDTD simulations were performed to calculate the electric field enhancement of the Au@PdPt SSs and to explore the underlying mechanism of the photocatalytic process. This study provides valuable insights for the design of novel high-performance photocatalysts.

2 | Results and Discussion

We selected AuNRs as the plasmonic core material for constructing multimetallic nanostructures, owing to their high purity and facile synthesis. AuNRs are a class of plasmonic nanomaterials whose LSPR can be readily tuned by adjusting their aspect ratio (length/diameter), enabling spectral modulation from approximately 600 nm to beyond 1200 nm. Following the dual-surfactant method reported by Ye et al. [44], we synthesized AuNRs via

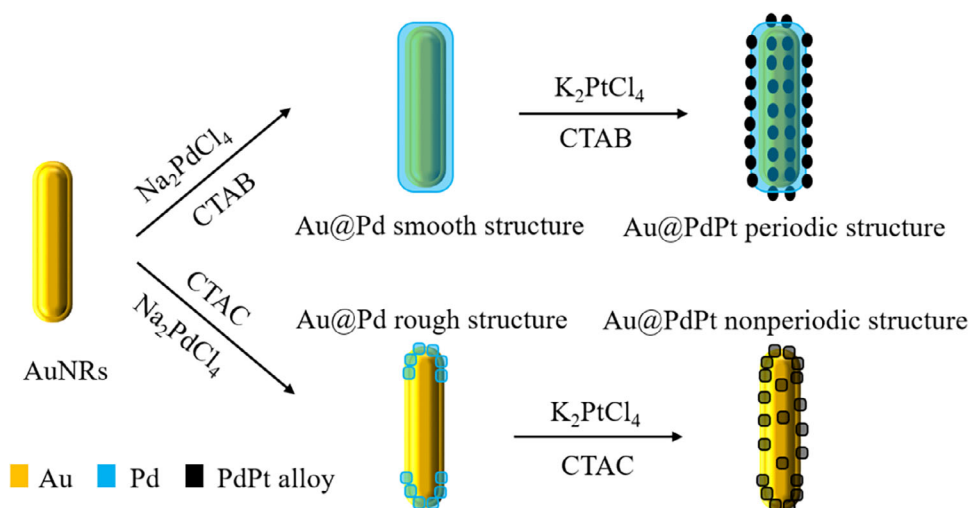
a seed-mediated growth approach, with minor modifications to the experimental details. The resulting AuNRs had an average length of 72.8 ± 7.1 nm and a width of 28.7 ± 3.1 nm, serving as the substrate for subsequent heterostructure growth. The transmission electron microscopy (TEM) images and UV-Vis-NIR spectra are shown in Figure S1.

In our experiments, we modulated the growth process by varying the type of surfactant present in the reaction solution, as illustrated in Scheme 1. Briefly, when Pd was grown on the AuNRs surface using CTAB as the surfactant, a smooth Pd layer was formed, denoted as the Au@Pd smooth structure. Subsequent growth of Pt on this structure, also using CTAB, led to the formation of periodically arranged PdPt alloy clusters via a surface corrosion and regrowth process, referred to as the Au@PdPt periodic structure. In contrast, when CTAC was used as the surfactant during Pd deposition, Pd preferentially grew at the ends of the AuNRs, forming a rough Pd layer, designated as the Au@Pd rough structure. Subsequent Pt deposition under the same CTAC conditions led to the formation of randomly arranged PdPt alloy clusters, referred to as the Au@PdPt nonperiodic structure.

Our results demonstrate that the choice of surfactant profoundly influences the deposition behavior of Pd and Pt on the AuNRs surface. Figure 1 displays the TEM, energy-dispersive X-ray spectroscopy (EDS), and high-resolution TEM (HRTEM) images of the Au@PdPt SSs synthesized using CTAB (Figure 1a–c) and CTAC (Figure 1d–f). The detailed EDS mapping images are shown in Figure S2.

When CTAB was used, the resulting Au@PdPt periodic structure exhibited a uniform distribution of PdPt alloy clusters on the AuNRs surface, as shown in Figure 1a. The EDS mapping images (Figure 1b; Figure S2a–d) confirm the homogeneous distribution of Pd and Pt, indicating alloy formation. The HRTEM image (Figure 1c) clearly reveals the lattice interface between the AuNRs core and the PdPt shell, with a measured interplanar spacing of 0.192 nm, corresponding to the Pd/Pt(100) lattice. In contrast, employing CTAC resulted in a non-periodic Au@PdPt structure where PdPt alloy clusters were predominantly deposited at the AuNRs termini (Figure 1d). EDS mapping images (Figure 1e; Figure S2e–h) confirm that Pd and Pt are concentrated at the nanorod tips. The HRTEM image (Figure 1f) again shows an interplanar spacing of 0.192 nm, consistent with the Pd/Pt(100) lattice.

To determine the oxidation states and degree of alloying for Pd and Pt in Au@PdPt, we employed X-ray photoelectron spectroscopy (XPS) to analyze the surface composition of the Au@PdPt (CTAB) sample. As shown in Figure S3, characteristic peaks for metallic gold were observed at binding energies of 82.4 eV (Au⁰4f_{7/2}) and 86 eV (Au⁰4f_{5/2}). Peaks corresponding to zero-valent palladium appeared at 333.7 and 338.8 eV, while those for zero-valent platinum were located at 69.6 and 72.9 eV. Notably, these binding energies for Pd and Pt exhibit slight negative shifts compared to commercial reference materials: Pd/C standard values (3d_{5/2}: 335.80 eV; 3d_{3/2}: 340.80 eV) and Pt/C standard values (4f_{7/2}: 71.30 eV; 4f_{5/2}: 74.30 eV) [45]. This deviation is likely attributable to electronic interactions within the Pd-Pt alloy shell.



SCHEME 1 | Schematic illustration of the synthesis of multimetallic Au@PdPt SSs on AuNRs using different surfactants. Under CTAB conditions, a smooth Pd shell followed by periodic PdPt alloy clusters is formed. Under CTAC conditions, Pd preferentially deposits at the nanorod ends, leading to randomly distributed PdPt clusters.

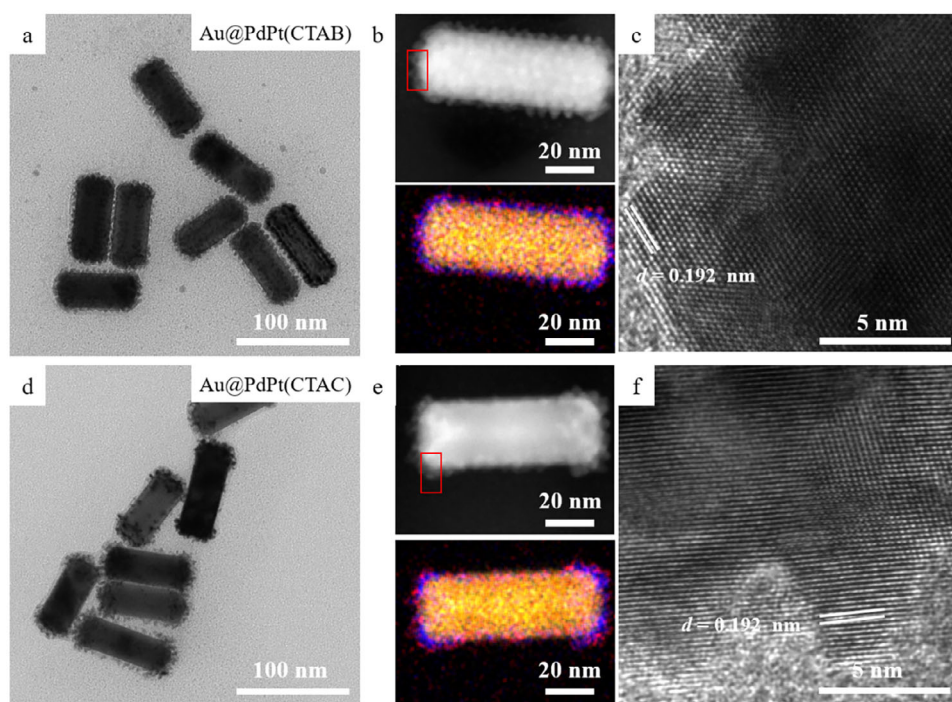


FIGURE 1 | Characterization of Au@PdPt SSs synthesized using CTAB and CTAC as surfactants. TEM, EDS mapping, and HRTEM images of Au@PdPt SSs synthesized with CTAB (a-c) and CTAC (d-f). (a) and (d) show TEM images, (b) and (e) show EDS mapping images, (c) and (f) show HRTEM images. In EDS mapping images, Au is shown in yellow, Pd in blue, and Pt in red.

To further investigate the intermediate product, Au@Pd, we performed characterization (Figure S1b–d). TEM images show that when CTAB was used, a smooth Pd shell was formed; whereas with CTAC, Pd primarily deposited at the ends of the AuNRs, forming discrete Pd nanoclusters. The extinction spectra (Figure S1d) reveal LSPR shifts in both cases: a slight redshift and broadening for Au@Pd(CTAB), with a new peak at 340 nm, and a more pronounced redshift and peak broadening for Au@Pd(CTAC), with overall increased absorbance.

However, the information obtained from electron microscopy is relatively limited, particularly for the Au@Pd nanostructures synthesized using CTAB as the surfactant, as shown in Figure S1b. In this case, the Pd shell is barely distinguishable on the nanorod surface. To gain further insight, we performed EDS characterization on the Au@Pd nanostructures synthesized with different surfactants, as shown in Figure S4. Figure S4a–d present the HAADF-STEM image and corresponding EDS mapping images for Au@Pd(CTAB), while Figure S4e–h show the corresponding images for Au@Pd(CTAC). In these images, yellow indicates the

Au element, and blue corresponds to Pd. From Figure S4a–d, it is evident that in the case of CTAB-mediated synthesis, a uniform and smooth Pd shell is formed on the AuNRs surface. In contrast, Figure S4e–h reveal that when CTAC is used as the surfactant, Pd preferentially deposits at the ends of the AuNRs, or more precisely, on regions with higher surface curvature, forming a larger number of discrete Pd nanoclusters.

Based on these findings, we attempted to synthesize nanomaterials using combinations of surfactants in different ratios. In the process of growing Pd on the surface of AuNRs, both CTAB and CTAC surfactants were introduced simultaneously. The ratio of CTAB to CTAC was varied while keeping the total volume of surfactants constant. This approach resulted in the synthesis of three different Au@Pd nanostructures. The TEM images and spectra of the Au@Pd nanostructures synthesized with varying surfactant ratios are shown in Figure S5. Figure S5a–c show the electron microscopy images of Au@Pd nanostructures synthesized with different CTAB/CTAC ratios of 3:1, 1:1, and 1:3, respectively. Analysis of these images reveals that when the proportion of CTAB is higher in the surfactant mixture, the synthesized Au@Pd nanostructures exhibit smoother surfaces, with Pd uniformly deposited on the AuNRs, forming a smooth and thin shell. In contrast, when the proportion of CTAC is higher, Pd predominantly deposits at the ends of the AuNRs, forming a small number of nanocrystal clusters at both ends. The extinction spectra shown in Figure S5d indicate that when the CTAB ratio is higher, the LSPR peak intensity is stronger, the peak width is narrower, and a new absorption peak at 340 nm is more prominent. When the CTAC ratio is higher, the LSPR peak intensity decreases, the peak width broadens, and there is a noticeable red shift in the peak position, with the absorption peak at 340 nm almost disappearing.

Subsequently, we continued the growth of Pt on the Au@Pd nanostructures under corresponding CTAB/CTAC ratios, ultimately synthesizing three different Au@PdPt SSs. Figure S6 shows the TEM images and spectra of Au@PdPt SSs synthesized with different surfactant ratios. Figure S6a–c present the electron microscopy images of Au@PdPt SSs synthesized with CTAB/CTAC ratios of 3:1, 1:1, and 1:3, respectively. Analysis of the images reveals that when the proportion of CTAB is higher, the PdPt clusters on the surface of the Au@PdPt SSs are evenly distributed across the AuNRs surface. In contrast, when the proportion of CTAC is higher, the PdPt clusters are primarily concentrated at the ends of the AuNRs, and their distribution appears irregularly. Analysis of the extinction spectra shown in Figure S6d indicates that as the CTAC ratio increases, the LSPR peak intensity enhances, and the peak position undergoes a red shift.

The influence of CTAB compared with CTAC on the morphology evolution of Au@PdPt structures proves critically important. Previous investigations reveal that in CTAB-dominant systems, ions preferentially adsorb onto both {100} and {111} crystal facets of AuNRs, promoting anisotropic growth along these planes—with {100} terminating at the poles and {111} encompassing the sides [46, 47]. This unique adsorption behavior enables uniform deposition of Pd layers across the entire AuNRs surface when CTAB prevails. Conversely, under CTAC-dominated conditions, ions exhibit selective affinity for the terminal {100} facets of

AuNRs, driving pronounced longitudinal anisotropic growth. Consequently, this preference leads to the formation of numerous discrete Pd nanoclusters predominantly localized at the AuNRs tips. Notably, Pt deposition follows a similar growth mechanism as Pd.

To investigate the photocatalytic activity of Au@PdPt SSs under plasmonic enhancement, we selected a model reaction system using sodium borohydride to reduce the MB solution and conducted experiments under both dark and xenon lamp illumination. During the reduction process, the color of the MB solution changes from blue to colorless.

In the photocatalytic reaction, we monitored and recorded the intensity of the characteristic extinction peak of the MB solution at 630 nm in the visible-near infrared spectra as a function of reaction time to reflect the photocatalytic rate. Specifically, at the beginning of the reaction ($t = 0$ min), the peak corresponding to the MB solution was measured as C_0 . Subsequently, at appropriate time intervals during the reaction, the peak at 630 nm was measured as C . The $-\ln(C/C_0)$ curve was then calculated, and the rapid rise phase of the curve was linearly fitted. The slope of the fitted line was used as the standard for determining the reaction rate. Figure S7a shows the raw data of the MB photocatalytic experiment without a catalyst, while Figure S7c,d display the raw data for AuNRs as a catalyst in MB photocatalytic experiments under both dark and light conditions. Figure 2 presents the fitted rate curves for the MB catalytic and photocatalytic experiments of Au@Pd and Au@PdPt SSs under both dark and light conditions. The corresponding raw data for the catalytic experiments (under dark) shown in Figure 2 are provided in Figure S8, while the raw data for the photocatalytic experiments (under light) are provided in Figure S9.

To better demonstrate the catalytic rates of different nanostructures, we quantified the slopes obtained from Figure 2 and plotted a bar chart, as shown in Figure 3. From the figure, it is evident that for all Au@Pd and Au@PdPt SSs, the catalytic rate under illumination is higher than that under dark conditions. Regardless of illumination, the catalytic rate of Au@Pd nanostructures is lower than that of Au@PdPt SSs. Under illumination, Au@PdPt synthesized with CTAB exhibits the highest rate among all experiments, with a rate that is 2.46 times higher than that of the same nanostructure under dark conditions, and it is significantly higher than that of other nanostructures. Detailed data can be found in Table S1.

To investigate the electric field distribution of the nanostructures at the MB peak wavelength of 630 nm, we conducted FDTD simulation studies on the Au@PdPt nanostructures synthesized using two different surfactants. In the FDTD simulations, we first modeled the AuNRs based on the dimensions obtained from the experiments, then applied a Pd shell or a series of PdPt nanoparticles on the surface of the AuNRs model, ultimately resulting in the desired simulation model. Figure 4a shows the experimental extinction spectra of the Au@PdPt SSs synthesized with two different surfactants, while Figure 4b presents the normalized far-field scattering spectra obtained from the FDTD simulations. Comparing the two, we observe that both the experimental and simulated spectra exhibit the same trend, with the peak position of the CTAC group showing a slight redshift

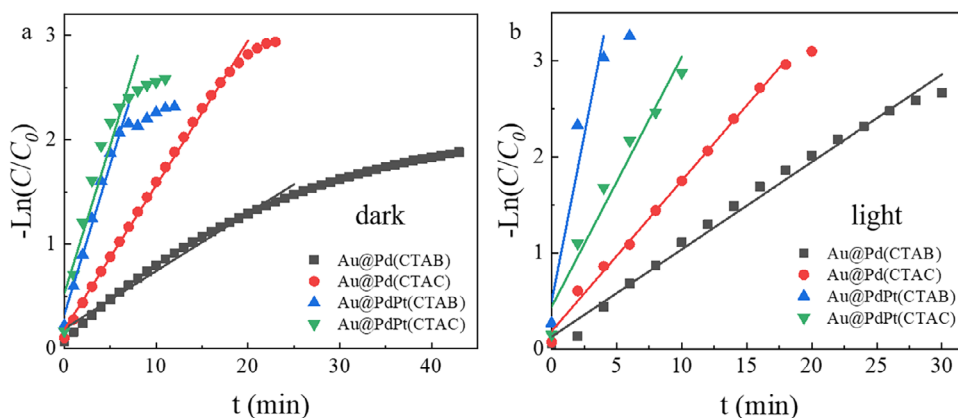


FIGURE 2 | Catalytic and photocatalytic performance of Au@Pd and Au@PdPt in the degradation of MB. (a) Catalytic fitted rate curves under dark conditions. (b) Photocatalytic fitted rate curves under light conditions.

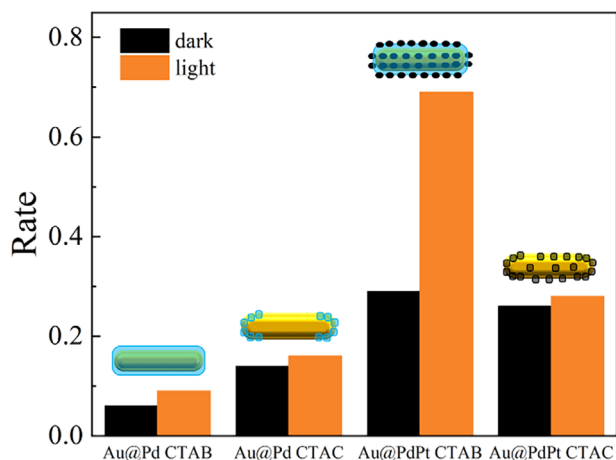


FIGURE 3 | Bar chart comparison of fitted rate slopes under light and dark conditions for different catalysts.

compared to the CTAB group. Figure 4c,d display the electric field intensity distribution maps obtained from the FDTD simulations. From these, it is evident that the electric field in the CTAB group is evenly distributed around the entire nanomaterial, whereas in the CTAC group, the electric field is concentrated at the two ends of the nanomaterial. This distribution corresponds to the growth patterns of Pd and Pt on the surface of the AuNRs.

Based on the above results, we propose that the catalytic performance of Au@PdPt consists of two main components. The surface layers of Pd and Pt act as the primary catalysts, with their catalytic performance originating from the inherent chemical catalytic properties of the materials. Gold, as the core, primarily provides plasmonic enhancement, where plasmon excitation under illumination generates a large amount of hot electrons that participate in the catalytic reaction. On the other hand, the surface structure significantly influences the catalytic reaction. Among the various structures, the Au@PdPt synthesized with CTAB, which exhibits a periodic structure, demonstrates the strongest catalytic and photocatalytic performance. This is due to the uniform distribution of the PdPt alloy shell on the surface, providing a larger contact area for catalysis, allowing the reactants to quickly and evenly interact with the Pd-Pt alloy catalyst. In contrast, the Au@PdPt synthesized with CTAC, which

exhibits a non-periodic structure, has a less uniform surface, reducing the contact opportunities with the reactant. Moreover, the periodic structure of Au@PdPt, when illuminated, generates a strong electric field due to its uniformity, releasing more hot electrons to facilitate catalysis. This phenomenon is absent in the non-periodic structure of Au@PdPt.

In the catalysis of Au@Pd, the Au@Pd structure with Pd grown at the tips, synthesized using CTAC, exhibits stronger catalytic performance compared to the core-shell structure of Au@Pd synthesized using CTAB. This is because the electric field induced by the LSPR effect of the AuNRs is concentrated at the two ends of the AuNRs. Since the electric field is concentrated at the ends of the AuNRs, and assuming that the precursor in the experiment undergoes complete reaction, the Au@Pd structure with Pd grown at the tips will have more Pd at the ends of the AuNRs. This results in enhanced catalytic effects, making the catalytic performance stronger than that of the core-shell structured Au@Pd synthesized using CTAB. It is crucial to note that our FDTD simulations reveal weaker localized electric fields in CTAB-synthesized Au@PdPt compared to CTAC counterparts. However, reduced field strength does not necessarily correlate with fewer hot carriers—electric field intensity depends strongly on both material structure and composition. Supporting evidence includes prior observations where gold nanobipyramids and nanorods showed comparable catalytic activity despite distinct field distributions [35, 48]. Similarly, in photocatalytic studies of Au@Ag compared with AuNRs, the enhanced internal field from silver did not translate into significantly improved performance relative to all-gold systems [35].

3 | Conclusions

In summary, we have successfully synthesized Au@PdPt core-shell superstructures using a seed-mediated method, where the Pd and Pt shell layers were sequentially deposited onto the pre-synthesized AuNRs surface. By controlling the type of surfactant, the growth behavior and periodic structure of the shell layers were effectively regulated. When CTAB was used as the surfactant, the resulting Au@PdPt SSs exhibited a periodic structure with the shell layer uniformly covering the entire nanorod surface. However, when CTAC was used, the Pd and Pt shell layers

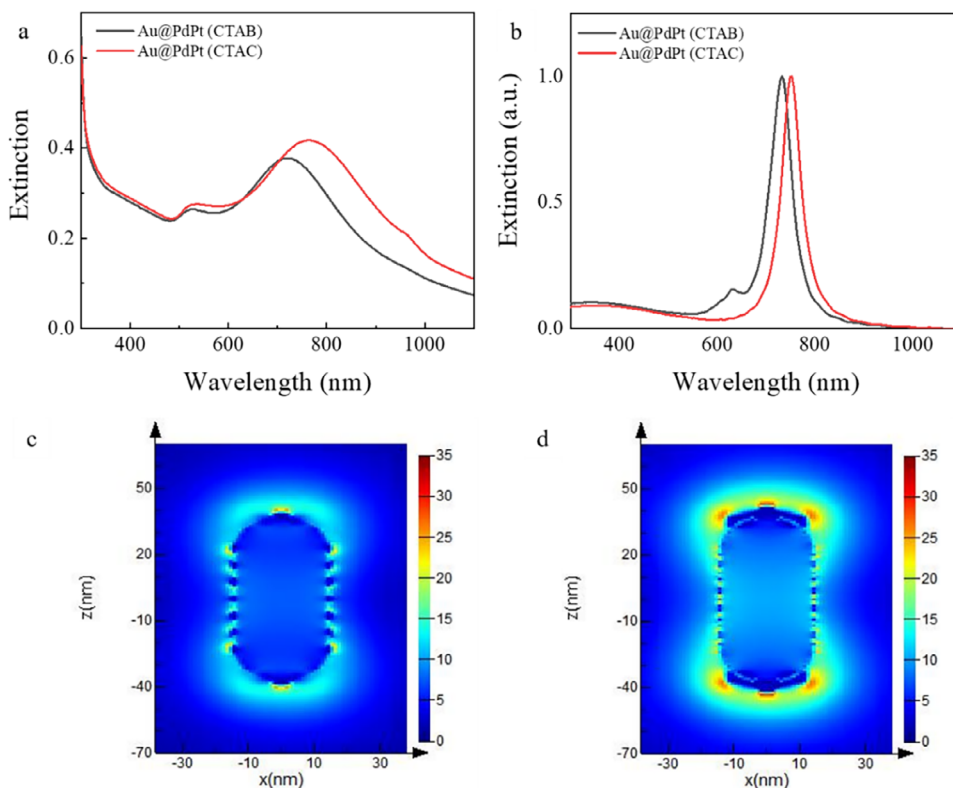


FIGURE 4 | Optical properties and FDTD simulation results of Au@PdPt SSs synthesized with different surfactants. (a) Experimental UV-Vis-NIR spectra of Au@PdPt SSs. (b) FDTD-simulated total scattering spectra of Au@PdPt SSs. (c,d) FDTD-simulated electric field intensity distributions for Au@PdPt (CTAB) (c) and Au@PdPt (CTAC) (d).

predominantly grew at the tips of the nanorods, forming a non-periodic structure. This structural difference is primarily attributed to the differing adsorption capacities of CTAB and CTAC on different crystal planes, which lead to different nucleation locations and growth directions during the metal precursor reduction process.

In the photocatalytic experiment of reducing MB with NaBH_4 , the Au@PdPt periodic structure synthesized with CTAB exhibited the best performance. Under visible light irradiation, its reaction rate was 2.38 times faster than under dark reaction conditions and 11.5 times faster than the Au@Pd sample synthesized with CTAB under dark conditions. This performance improvement can be attributed to the LSPR effect of the Au core, which effectively promotes the generation and transfer of hot electrons, while the PdPt alloy shell provides efficient catalytic sites. The periodic structure contributes to a more uniform charge distribution and more efficient interfacial electron transfer, which is superior to the non-periodic structure with shell layers only distributed at the tips.

To further elucidate the plasmonic characteristics of the Au@PdPt SSs, FDTD simulations were conducted. The results demonstrated that the electric field distribution of the CTAB-synthesized Au@PdPt exhibited a uniform enhancement around the entire nanorod surface, whereas the CTAC-synthesized nanostructure showed strong field localization at the rod tips. This observation is consistent with the experimentally observed shell morphologies and confirms that the periodic shell structure

facilitates a broader and more uniform plasmonic enhancement, which is beneficial for light-driven catalytic processes.

This study reveals that the type of surfactant can precisely control the structures and photocatalytic performances of multimetallic nanostructures, providing new design ideas for constructing efficient plasmon-driven photocatalysts.

4 | Experimental Section

4.1 | Materials

Hexadecyltrimethylammonium bromide (CTAB, >99.0%), L-ascorbic acid (AA, >99.99%), Chloroauric acid (HAuCl_4), hydrochloric acid (HCl, 37 wt.% in water), and methyl blue (MB) were purchased from Shanghai Macklin Biochemical Technology Co., Ltd. Hexadecyltrimethylammonium chloride (CTAC, >99.0%), sodium borohydride (NaBH_4 , 98%), sodium oleate (NaOL, >99.8%), silver nitrate (AgNO_3 , >99.8%), Sodium tetrachloropalladate (II) (Na_2PdCl_4 , >99.99%), and Potassium tetrachloroplatinate (II) (K_2PtCl_4 , >99.99%) were purchased from Shanghai Aladdin Biochemical Technology Co. Ltd. Ultrapure water (Millipore Milli-Q grade, 18.2 M Ω) was used in all of the experiments. All chemicals were used as received without further purification. All glassware for the synthesis of AuNRs was cleaned with freshly prepared aqua regia (HCl/ HNO_3 in a 3:1 v/v), rinsed with a large amount of water, and dried in an oven at 60°C before usage.

4.2 | Synthesis of AuNRs

AuNRs with an aspect ratio of 2.6 were prepared by following a seed-mediated growth procedure previously reported by Murray et al. [44] The seed solution for AuNRs growth was prepared as follows: firstly, 0.25 mL 10.0 mM HAuCl₄ was added to 10.0 mL 0.1 M CTAB solution. Then 0.6 mL 10.0 mM NaBH₄ (freshly prepared with cold water) was added to the solution above under the vigorous stirring (1200 rpm) and was stopped after 2 min. The color of the solution changed from light yellow to brownish. Finally, the seed solution was aged at 30°C for 30 min before use.

To prepare the growth solution, 7.0 g (~37 mM in the final growth solution) of CTAB and 1.24 g NaOL were mixed in 250 mL of warm water (50°C). 18.0 mL 4.0 mM AgNO₃ was added to the solution and kept undisturbed at 30°C for 15 min. Afterward, 250 mL 1.0 mM of HAuCl₄ solution was added and stirred at 700 rpm. The result solution became colorless after 90 min. Then 2.1 mL of HCl (37 wt. % in water) was injected and stirred at 700 rpm for 15 min. After 15 min, 1.25 mL 64.0 mM of ascorbic acid was added to the solution above and kept vigorously stirring for 30 sec before the addition of 0.8 mL of the seed solution. The resulted mixture was stirred for 30 s and left undisturbed at 30°C for 12 h for AuNRs growth.

4.3 | Synthesis of Au@PdPt SSs

The as-prepared AuNRs solution was purified twice by centrifugation at 7000 rpm for 30 min followed by removal of the supernatant. The resulted solution (concentrated 10 times) was kept in 2.0 mM of CTAB as the stock solution. To deposit Pd on the surface of AuNRs, 0.1 mL of the AuNRs stock solution was added into 3.4 mL of 30.0 mM CTAB at room temperature (25°C). Then 0.05 mL of 100 mM AA and 0.04 mL of 2.0 mM Na₂PdCl₄ were added into the solution, and left undisturbed for 10 min. Then the Au@Pd core-shell nanostructures can be obtained. Finally, 0.04 mL 2.0 mM K₂PtCl₄ were added into the Au@Pd solution, and kept in a 60°C water bath for 20 min. Final products were collected by two centrifugation cycles at 7000 rpm for 20 min and redispersed in water for further use.

To synthesize the Au@PdPt in CTAC, 0.1 mL of the AuNRs stock solution was added into 3.4 mL of 30.0 mM CTAC at room temperature (25°C). Then 0.05 mL of 100 mM AA and 0.04 mL of 2.0 mM Na₂PdCl₄ were added into the solution, and left undisturbed for 10 min. Then the Au@Pd core-shell nanostructures can be obtained. Finally, 0.04 mL 2.0 mM K₂PtCl₄ were added into the Au@Pd solution, and kept in a 60°C water bath for 20 min. Final products were collected by two centrifugation cycles at 7000 rpm for 20 min and redispersed in water for further use. To test the effect of the CTAB/CTAC ratio on the final morphologies of Au@PdPt SSs, we used the CTAC/CTAB ratio of 1:3, 1:1, 3:1 in the experiments.

4.4 | Catalysis

1.0 mL of 0.05 mM MB were mixed with 0.03 mL of 0.05 M freshly prepared NaBH₄, then different kinds of Au@PdPt (0.01 mL)

solution or 0.01 mL AuNRs solution were added into the mixed solution. We measured the extinction spectra of the solution at 1 min intervals until the peak corresponding to 630 nm disappeared. After the reaction, the color of the solution changes from blue to transparent.

4.5 | Photocatalysis

1.0 mL of 0.05 mM MB were mixed with 0.03 mL of 0.05 M freshly prepared NaBH₄, then different kinds of Au@PdPt (0.01 mL) solution or 0.01 mL AuNRs solution were added into the mixed solution. We used the above catalytic experimental steps on the basis of the illumination with a 250 W Xenon lamp (HDL-II, Suzhou Betical Optoelectronics Technology Co. Ltd, China), equipped with a long pass filter ($\lambda > 420$ nm). We measured the extinction spectra of the solution at two-minute intervals until the peak at 630 nm disappeared. The MB concentration was determined at the wavelength of 630 nm using a UV-Vis-NIR spectrophotometer (UV-1900i, Shimadzu). The reaction was maintained at normal atmospheric temperature.

4.6 | Characterization

UV-Vis-NIR extinction spectra were collected by a UV-1900i Spectrophotometer (SHIMADZU, Japan), with a 10-mm optical path. The TEM images were operated on a HT-7700 microscope (HITACHI, Japan) operating at a voltage of 100 kV. The particle sizes of the nanoparticles were measured from TEM images using imageJ software, whereby > 100 nanoparticles were measured for each sample. HRTEM images, HAADF-STEM imaging, and EDS mapping were performed using a FEI Talos F200S with an acceleration voltage of 200 kV.

4.7 | FDTD Simulation

FDTD is a method for solving Maxwell's equations on a discretized spatial grid in complex geometries. The FDTD simulations were carried out using Lumerical Solutions, a commercially available FDTD simulation software package. Simulations were performed in 3D layout, with a unit cell of 1000 nm×1000 nm×1000 nm along the x-axis, the y-axis, and the z-axis, respectively. Perfectly matched layers in 3D were used as boundary conditions. A total field scattered field (TFSF) light source was used to simulate a propagating plane wave interacting with the nanostructures, with the range of 300–1100 nm injecting into the unit cell along the +y direction. A three-dimensional nonuniform mesh was used, and the mesh size was set to be 1 nm. The shape and size of Au@PdPt and AuNRs were determined from the corresponding TEM images. The dielectric functions of Au was obtained by fitting the points from the data of Palik [49], and the dielectric function of Pd and Pt were obtained from the data of Werner et al. [50]. We calculated the effective dielectric functions of PdPt alloy by the effective medium approximation (EMA) based on the Maxwell-Garnett equation [51]

$$P \frac{\varepsilon_{eff} - \varepsilon_{Pd}}{\varepsilon_{eff} + 2\varepsilon_{Pd}} + (1 - P) \frac{\varepsilon_{Pt} - \varepsilon_{Pd}}{\varepsilon_{Pt} + 2\varepsilon_{Pd}} = 0 \quad (1)$$

Thus, the effective dielectric functions of PdPt alloy is given by

$$\varepsilon_{eff} = \varepsilon_{Pd} \frac{2P(\varepsilon_{Pt} - \varepsilon_{Pd}) + \varepsilon_{Pt} + 2\varepsilon_{Pd}}{2\varepsilon_{Pd} + \varepsilon_{Pt} - P(\varepsilon_{Pt} - \varepsilon_{Pd})} \quad (2)$$

where ε_{Pd} , ε_{Pt} , and ε_{eff} are the dielectric functions of the Pt, Pd, and composite system (PdPt alloy), respectively. P is the proportion of Pt in the PdPt alloy, which could be obtained from the EDS mapping (P = 22% for PdPt superstructures). Once the ε_{eff} was calculated by Equation 2, it was imported into the FDTD software. The real and imaginary part of the ε_{eff} was drawn in Figure S10.

Acknowledgements

The authors thank Sudan Shen for her assistance in TEM at State Key Laboratory of Chemical Engineering (Zhejiang University). T. S. Deng acknowledge financial support from Zhejiang Provincial Natural Science Foundation (Grant: LY24F050008) and National Natural Science Foundation of China (NSFC, Grant: 61905056). This work was also supported in part by Shanghai Industrial Collaborative Innovation Project under grant HCXBCY-2024-051.

Conflicts of Interest

The authors declare no conflicts of interest.

Data Availability Statement

The data that support the findings of this study are available in the supplementary material of this article.

References

1. Z. A. C. Ramli, J. Pasupuleti, N. F. H. N. Zaiman, et al., "Evaluating Electrocatalytic Activities of Pt, Pd, Au and Ag-Based Catalyst On PEMFC Performance: A Review," *International Journal of Hydrogen Energy* 104 (2025): 463–486, <https://doi.org/10.1016/j.ijhydene.2024.04.177>.
2. M. J. Saadh, W. A. Khidr, K. H. Alfarttoosi, et al., "Metal Nanoparticles As A Promising Therapeutic Approach For Prostate Cancer Diagnosis And Therapy: A Comprehensive Review," *Medical Oncology* 42 (2025): 83, <https://doi.org/10.1007/s12032-025-02633-4>.
3. A. Sati, T. N. Ranade, S. N. Mali, H. K. A. Yasin, and A. Pratap, "Silver Nanoparticles (AgNPs): Comprehensive Insights Into Bio/Synthesis, Key Influencing Factors, Multifaceted Applications, and Toxicity—A 2024 Update," *ACS Omega* 10, no. 8 (2025): 7549–7582, <https://doi.org/10.1021/acsomega.4c11045>.
4. N. G. Khlebtsov, L. A. Dykman, and B. N. Khlebtsov, "Synthesis and Plasmonic Tuning Of Gold And Gold–Silver Nanoparticles," *Russian Chemical Reviews* 91 (2022): RCR5058, <https://doi.org/10.57634/RCR5058>.
5. Y. Hang, A. Wang, and N. Wu, "Plasmonic Silver And Gold Nanoparticles: Shape- And Structure-Modulated Plasmonic Functionality For Point-Of-Caring Sensing, Bio-Imaging And Medical Therapy," *Chemical Society Reviews* 53 (2024): 2932–2971, <https://doi.org/10.1039/D3CS00793F>.
6. S.-L. Ke, C.-X. Kan, B. Mo, B. Cong, and J.-J. Zhu, "Research Progress On The Optical Properties Of Gold Nanorods," *Acta Physico-Chimica Sinica* 28 (2012): 1275.
7. L. Meng, J. Zhang, H. Li, W. Zhao, and T. Zhao, "Preparation and Progress in Application of Gold Nanorods," *Journal of Nanomaterials* 2019 (2019): 1, <https://doi.org/10.1155/2019/4925702>.
8. N. Miryousefi, M. Varmazyad, and F. Ghasemi, "Synthesis of Au@Ag Core-Shell Nanorods With Tunable Optical Properties," *Nanotechnology* 35 (2024): 395605, <https://doi.org/10.1088/1361-6528/ad572b>.
9. L. Zhou, Q. J. Huang, and Y. N. Xia, "Plasmon-Induced Hot Electrons in Nanostructured Materials: Generation, Collection, and Application to Photochemistry," *Chemical Reviews* 124 (2024): 8597–8619, <https://doi.org/10.1021/acs.chemrev.4c00165>.
10. K. A. Dahan, Y. Li, J. Xu, and C. X. Kan, "Recent Progress Of Gold Nanostructures And Their Applications," *Physical Chemistry Chemical Physics* 25 (2023): 18545–18576, <https://doi.org/10.1039/D3CP01549A>.
11. J. T. Su, X. Q. Hou, N. Dai, and Y. Li, "Localized Surface Plasmon Resonance Enhanced Photodetector: Physical Model, Enhanced Mechanism And Applications," *Frontiers of Physics* 19 (2024): 63501, <https://doi.org/10.1007/s11467-024-1413-8>.
12. D. J. Roth, A. V. Krasavin, and A. V. Zayats, "Nanophotonics With Plasmonic Nanorod Metamaterials," *Laser & Photonics Reviews* 18 (2024): 2300886, <https://doi.org/10.1002/lpor.202300886>.
13. E. X. Tan, Q.-Z. Zhong, J. R. Ting Chen, et al., "Surface-Enhanced Raman Scattering-Based Multimodal Techniques: Advances and Perspectives," *ACS Nano* 18 (2024): 32315–32334, <https://doi.org/10.1021/acsnano.4c12996>.
14. C. Wen, L. Wang, L. Liu, X.-C. Shen, and H. Chen, "Surface-Enhanced Raman Probes Based on Gold Nanomaterials for in vivo Diagnosis and Imaging," *Chemistry – An Asian Journal* 17 (2022): 202200014, <https://doi.org/10.1002/asia.202200014>.
15. L. T. Dang, H. L. Nguyen, H. V. Pham, and M. T. T. Nguyen, "Shell Thickness-Controlled Synthesis of Au@Ag Core-Shell Nanorods Structure For Contaminants Sensing by SERS," *Nanotechnology* 33 (2022): 075704, <https://doi.org/10.1088/1361-6528/ac201a>.
16. G. L. Wu, T. S. Deng, K. P. Wang, et al., "Synthesis of lipophilic Gold Nanorod Superparticles And Their Size-Dependent SERS Performances," *Journal of Nanoparticle Research* 27 (2025): 19, <https://doi.org/10.1007/s11051-025-06216-2>.
17. W.-F. Huang, H.-B. Xu, S.-C. Zhu, Y. He, H.-Y. Chen, and D.-W. Li, "Core-Shell Gold Nanoparticles@Pd-Loaded Covalent Organic Framework for In Situ Surface-Enhanced Raman Spectroscopy Monitoring of Catalytic Reactions," *ACS Sensors* 9, no. 5 (2024): 2421–2428, <https://doi.org/10.1021/acssensors.4c00103>.
18. A. Phengdaam, S. Phetsang, S. Jonai, K. Shinbo, K. Kato, and A. Baba, "Gold Nanostructures/Quantum Dots For The Enhanced Efficiency of Organic Solar Cells," *Nanoscale Advances* 6, no. 14 (2024): 3494–3512, <https://doi.org/10.1039/D4NA00016A>.
19. D. F. Carvalho, J. P. Teixeira, P. M. P. Salome, P. A. Fernandes, and M. R. P. Correia, "Gold Nanorods As Performance Enhancers In Planar Perovskite Solar Cells: A Numerical Study," *Solar Energy Materials and Solar Cells* 277 (2024): 113112, <https://doi.org/10.1016/j.solmat.2024.113112>.
20. Y. Hui, E.-M. You, Q.-P. Luo, et al., "Efficient Plasmon-Enhanced Perovskite Solar Cells By Molecularly Isolated Gold Nanorods," *Journal of Energy Chemistry* 73 (2022): 60–67, <https://doi.org/10.1016/j.jchem.2022.05.015>.
21. W. He, G. Ma, Q. Shen, and Z. Tang, "Engineering Gold Nanostructures for Cancer Treatment: Spherical Nanoparticles, Nanorods, and Atomically Precise Nanoclusters," *Nanomaterials* 12 (2022): 1738, <https://doi.org/10.3390/nano12101738>.
22. J. Ye, Q. Wen, Y. Wu, et al., "Plasmonic Anisotropic Gold Nanorods: Preparation And Biomedical Applications," *Nano Research* 15 (2022): 6372–6398, <https://doi.org/10.1007/s12274-022-4191-z>.
23. Y. Y. Bu, R. Q. Huang, Z. Li, et al., "Anisotropic Truncated Octahedral Au With Pt Deposition on Arris for Localized Surface Plasmon Resonance-Enhanced Photothermal and Photodynamic Therapy of Osteosarcoma," *ACS Applied Materials & Interfaces* 13 (2021): 35328–35341, <https://doi.org/10.1021/acsami.1c07181>.
24. S. Hajebi, M. Chamanara, S. S. Nasiri, et al., "Advances in Stimuli-Responsive Gold Nanorods For Drug-Delivery And Targeted Therapy Systems," *Biomedicine & Pharmacotherapy* 180 (2024): 117493, <https://doi.org/10.1016/j.biopha.2024.117493>.

25. M. Hajfathalian, K. J. Mossburg, A. Radaic, et al., "A Review Of Recent Advances In The Use Of Complex Metal Nanostructures For Biomedical Applications From Diagnosis To Treatment," *WIREs Nanomedicine and Nanobiotechnology* 16 (2024): 1959e, <https://doi.org/10.1002/wnan.1959>.
26. S. Li, Q. Ding, L. Zhang, et al., "Gold core@CeO₂ Halfshell Janus Nanocomposites Catalyze Targeted Sulfate Radical For Periodontitis Therapy," *Journal of Controlled Release* 370 (2024): 600–613, <https://doi.org/10.1016/j.jconrel.2024.05.016>.
27. C. Han, M.-Y. Qi, Z.-R. Tang, J. Gong, and Y.-J. Xu, "Gold Nanorods-Based Hybrids With Tailored Structures For Photoredox Catalysis: Fundamental Science, Materials Design And Applications," *Nano Today* 27 (2019): 48–72, <https://doi.org/10.1016/j.nantod.2019.05.001>.
28. P. Prielcel, H. A. Salami, R. H. Padilla, Z. Zhong, and J. A. Lopez-Sanchez, "Anisotropic Gold Nanoparticles: Preparation And Applications In Catalysis," *Chinese Journal of Catalysis* 37 (2016): 1619–1650, [https://doi.org/10.1016/S1872-2067\(16\)62475-0](https://doi.org/10.1016/S1872-2067(16)62475-0).
29. B. Wu, D. Liu, S. Mubeen, T. T. Chuong, M. Moskovits, and G. D. Stucky, "Anisotropic Growth of TiO₂ Onto Gold Nanorods For Plasmon-Enhanced Hydrogen Production From Water Reduction," *Journal of the American Chemical Society* 138 (2016): 1114–1117, <https://doi.org/10.1021/jacs.5b11341>.
30. G. Pandey, S. D. Lawaniya, S. Kumar, P. K. Dwivedi, and K. Awasthi, "A Highly Selective, Efficient Hydrogen Gas Sensor Based On Bimetallic (Pd–Au) Alloy Nanoparticle (NP)-Decorated SnO₂ Nanorods," *Journal of Materials Chemistry A* 11 (2023): 26687–26697, <https://doi.org/10.1039/D3TA05878F>.
31. J. Xu, H. Y. Xu, L. H. Xu, et al., "Plasmonic and Catalytic Au NBP@AgPd Nanoframes For Highly Efficient Photocatalytic Reactions," *Physical Chemistry Chemical Physics* 25 (2023): 13189–13197, <https://doi.org/10.1039/D3CP01153D>.
32. F. X. Tong, X. Z. Liang, X. L. Bao, and Z. K. Zheng, "Photocatalysis on Hybrid Plasmonic Nanomaterials: From Catalytic Mechanism Study at Single-Particle Level to Materials Design," *ACS Catalysis* 14 (2024): 11425–11446, <https://doi.org/10.1021/acscatal.4c03566>.
33. M. Lv, X. X. Zhang, B. Li, B. B. Huang, and Z. K. Zheng, "Single-Particle Fluorescence Spectroscopy for Elucidating Charge Transfer and Catalytic Mechanisms on Nanophotocatalysts," *ACS Nano* 18 (2024): 30247–30268, <https://doi.org/10.1021/acsnano.4c10702>.
34. A. Vijeata, A. W. Wark, G. R. Chaudhary, and S. Chaudhary, "Experimental and Theoretical Exploration Of Bactericidal And Photocatalytic Activities Of Hierarchically Porous AuNRs@CuO Nanocomposite," *Journal of Cleaner Production* 476 (2024): 143740, <https://doi.org/10.1016/j.jclepro.2024.143740>.
35. Q. Zhang, T. S. Deng, Y. Q. Dou, et al., "Trimetallic Nanostructures of Silver–Platinum Alloy Shells on Gold Nanorods for Plasmon-Mediated Photocatalysis," *ACS Applied Nano Materials* 5 (2022): 17048–17058, <https://doi.org/10.1021/acsnm.2c03953>.
36. Y. Q. Dou, Q. Zhang, T. S. Deng, Z. Q. Cheng, and X. Y. Zhao, "Deposition of Pd–Pt alloy zigzag shell Over Au Nanorods For Boosted Catalysis And Thermo-Photo Catalysis," *Journal of Materials Science* 59 (2024): 2302–2314, <https://doi.org/10.1007/s10853-024-09351-8>.
37. Z. J. Yong, Q. Q. Shi, R. F. Fu, and W. L. Cheng, "Fine-Tuning Au@Pd Nanocrystals for Maximum Plasmon-Enhanced Catalysis," *Advanced Materials Interfaces* 8 (2021): 2001686, <https://doi.org/10.1002/admi.202001686>.
38. Q. Gu, J. Zhu, G. J. Weng, J. J. Li, Y. B. Guo, and J. W. Zhao, "Au@AgPt Core/Cage Nanoframes As Photothermal Catalyst For Enhanced NIR-Induced 4-Nitrophenol Reduction," *Journal of Environmental Chemical Engineering* 12 (2024): 113273, <https://doi.org/10.1016/j.jece.2024.113273>.
39. J. L. Zhuo, G. G. Zhang, Y. Y. Ma, et al., "Seeded Growth of wavy Au@PdAu Core-Shell Nanoplates With Tunable Thickness For Visible Light-Assisted Reduction of 4-Nitrophenol," *Journal of Nanoparticle Research* 23 (2021): 256, <https://doi.org/10.1007/s11051-021-05361-8>.
40. N. Meir, I. J.-L. Plante, K. Flomin, et al., "Studying the Chemical, Optical And Catalytic Properties Of Noble Metal (Pt, Pd, Ag, Au)–Cu₂O Core–Shell Nanostructures Grown Via A General Approach," *Journal of Materials Chemistry A* 1 (2013): 1763–1769, <https://doi.org/10.1039/C2TA00721E>.
41. J. E. S. van der Hoeven, T. S. Deng, W. Albrecht, et al., "Structural Control Over Bimetallic Core–Shell Nanorods for Surface-Enhanced Raman Spectroscopy," *ACS Omega* 6 (2021): 7034–7046, <https://doi.org/10.1021/acsomega.0c06321>.
42. V. Sharma, N. Sinha, S. Dutt, M. Chawla, and P. F. Siril, "Tuning the Surface Enhanced Raman Scattering And Catalytic Activities Of Gold Nanorods By Controlled Coating Of Platinum," *Journal of Colloid and Interface Science* 463 (2016): 180–187, <https://doi.org/10.1016/j.jcis.2015.10.036>.
43. M. P. Perich, C. R. O'Connor, K. M. Draijer, et al., "In Situ Analysis Of Gas Dependent Redistribution Kinetics In Bimetallic Au–Pd Nanoparticles," *Journal of Materials Chemistry A* 12 (2024): 32760–32774, <https://doi.org/10.1039/D4TA03030C>.
44. X. Ye, C. Zheng, J. Chen, Y. Gao, and C. B. Murray, "Using Binary Surfactant Mixtures To Simultaneously Improve the Dimensional Tunability and Monodispersity in the Seeded Growth of Gold Nanorods," *Nano Letters* 13 (2013): 765–771, <https://doi.org/10.1021/nl304478h>.
45. W. K. Liang, Y. W. Wang, L. Zhao, et al., "Lithium Metal Electrode With Increased Air Stability and Robust Solid Electrolyte Interphase Realized by Silane Coupling Agent Modification," *Advanced Materials* 33 (2021): 2008133.
46. Y. F. Huang, K. M. Huang, and H. T. Chang, "Synthesis and Characterization of Au core–Au–Ag Shell Nanoparticles From Gold Seeds: Impacts Of Glycine Concentration and pH," *Journal of Colloid and Interface Science* 301 (2006): 145–154, <https://doi.org/10.1016/j.jcis.2006.04.079>.
47. V. Thambi, A. R. S. Gautam, and S. Khatua, "Core-shell Au@AuAg Nano-Peanuts For The Catalytic Reduction Of 4-Nitrophenol: Critical Role Of Hollow Interior And Broken Shell Structure," *Nanoscale Advances* 2, no. 10 (2020): 4841–4852, <https://doi.org/10.1039/D0NA00312C>.
48. E. J. Zhang, T. S. Deng, Y. C. Cheng, et al., "Gold Nanobipyramids Coated With Silver–Platinum Alloy Shells for Plasmonically Enhanced Photocatalytic Degradation of Methyl Orange," *ACS Applied Nano Materials* 7 (2024): 14596–14608, <https://doi.org/10.1021/acsnm.4c02124>.
49. E. D. Palik, *Handbook of Optical Constants of Solids*, (Academic Press, 1997).
50. W. S. M. Werner, K. Glantschnig, and C. Ambrosch-Draxl, "Optical Constants and Inelastic Electron-Scattering Data for 17 Elemental Metals," *Journal of Physical and Chemical Reference Data* 38 (2009): 1013–1092, <https://doi.org/10.1063/1.3243762>.
51. G. J. C. Maxwell, "Xii. Colours in Metal Glasses And In Metallic Films. Philosophical Transactions Of The Royal Society Of London A," *Mathematical, Physical and Engineering Sciences* 203 (1904): 359–371.

Supporting Information

Additional supporting information can be found online in the Supporting Information section.

Supporting file: ppsc70045-sup-0001-SuppMat.docx

Gold Nanorods Coated with Palladium-Platinum Alloy Shell Superstructures for Enhanced Plasmon-Driven Photocatalysis

Zhen-Ming Shen¹, Jie Liu^{1,}, Qi Zhang¹, Er-Ji Zhang¹, Xiaoyu Zhao², Yiqiang Gao^{1,*}, Zhigang Zhou¹, and
Tian-Song Deng^{1,*}*

*¹School of Electronics and Information Engineering, Hangzhou Dianzi University, Hangzhou 310018, P. R.
China.*

*²College of Materials and Environmental Engineering, Hangzhou Dianzi University, Hangzhou 310018, P. R.
China.*

**Corresponding author. E-mail: dengts@pku.edu.cn, yqgao@hdu.edu.cn, liujie4209@hdu.edu.cn*

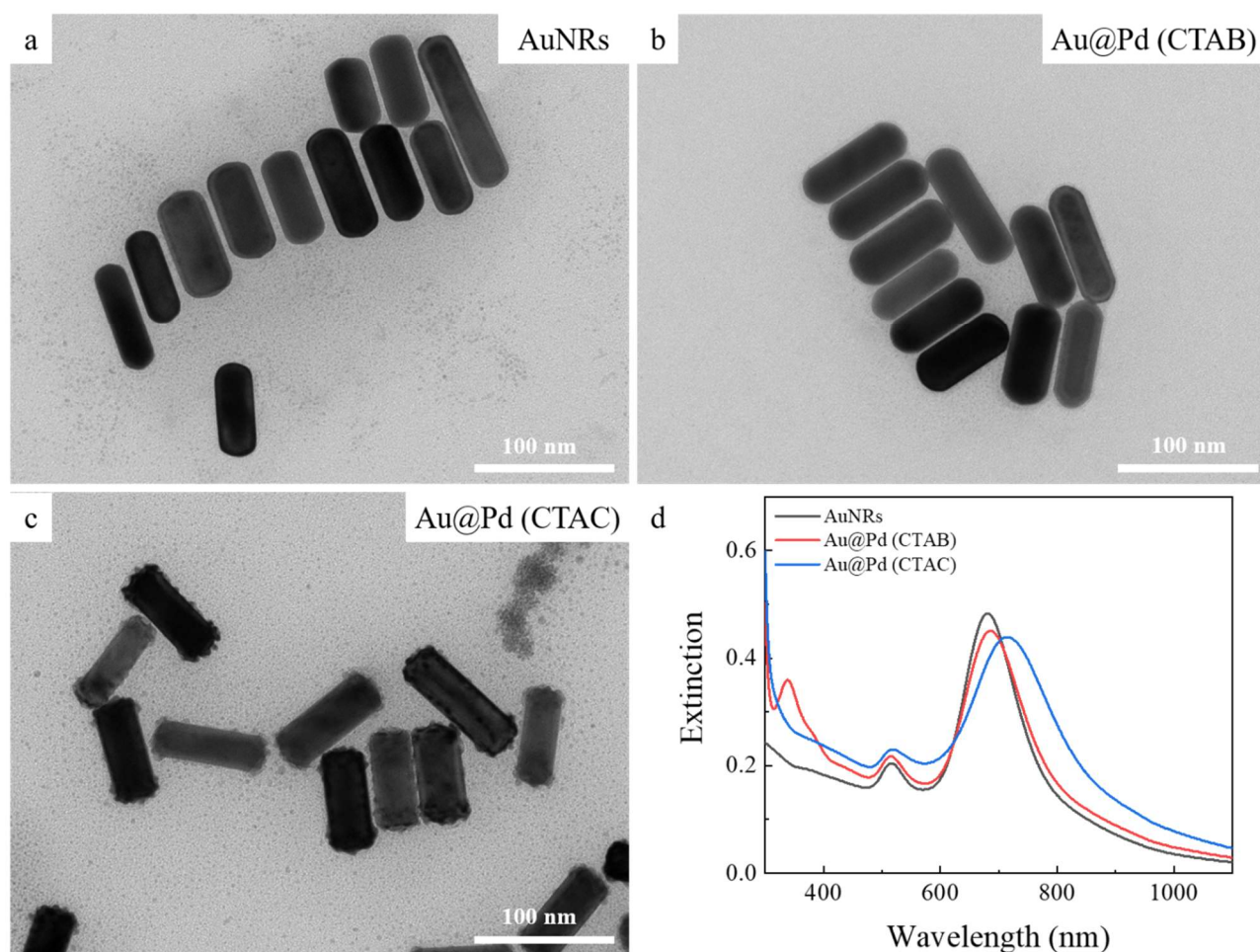


Figure S1. TEM images and UV-vis spectra of AuNRs and Au@Pd nanostructures. (a) TEM image of AuNRs. (b) TEM image of Au@Pd (CTAB). (c) TEM image of Au@Pd (CTAC). (d) UV-vis spectra of AuNRs, Au@Pd (CTAB), and Au@Pd (CTAC).

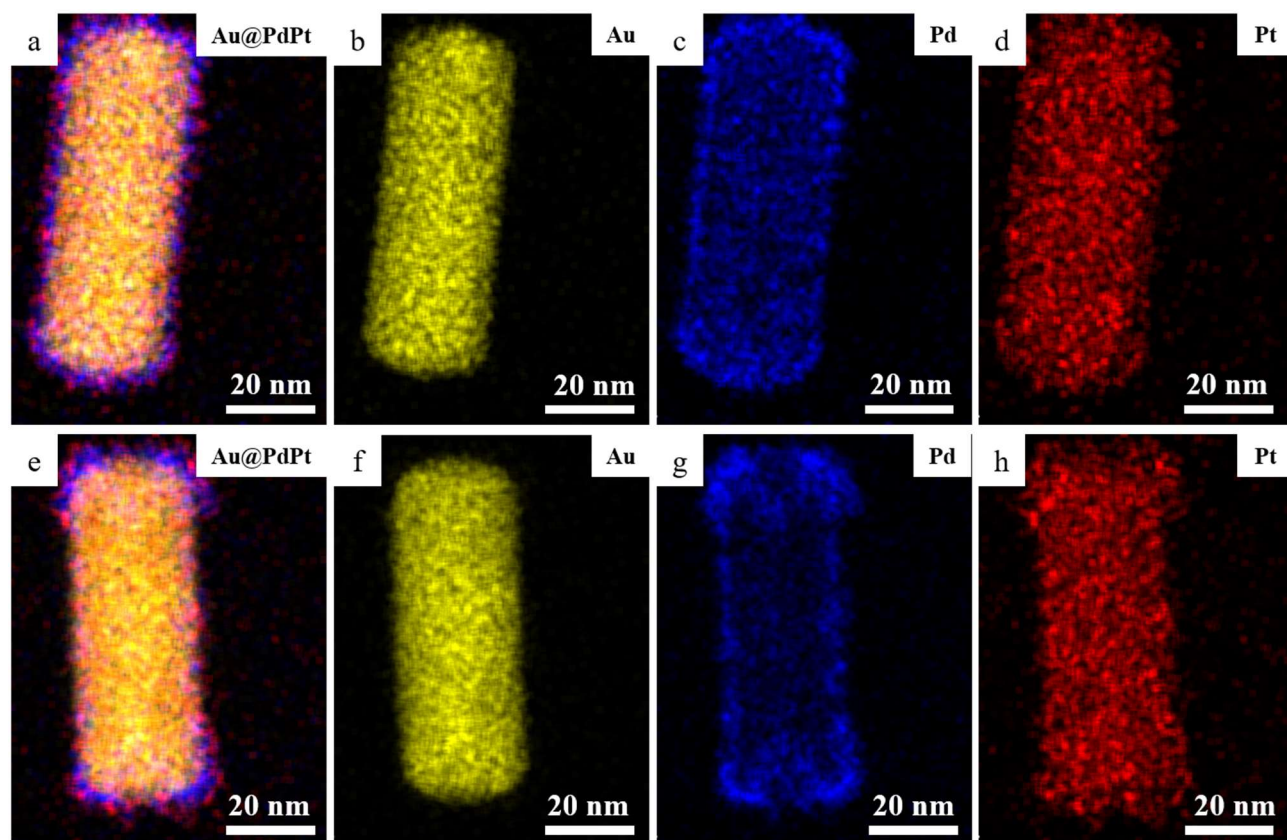


Figure S2. EDS mapping images of Au@PdPt SSs synthesized with different surfactants.(a-d) EDS mapping images of Au@PdPt (CTAB); (e-h) EDS mapping images of Au@PdPt (CTAC). Au is shown in yellow, Pd in blue, and Pt in red.

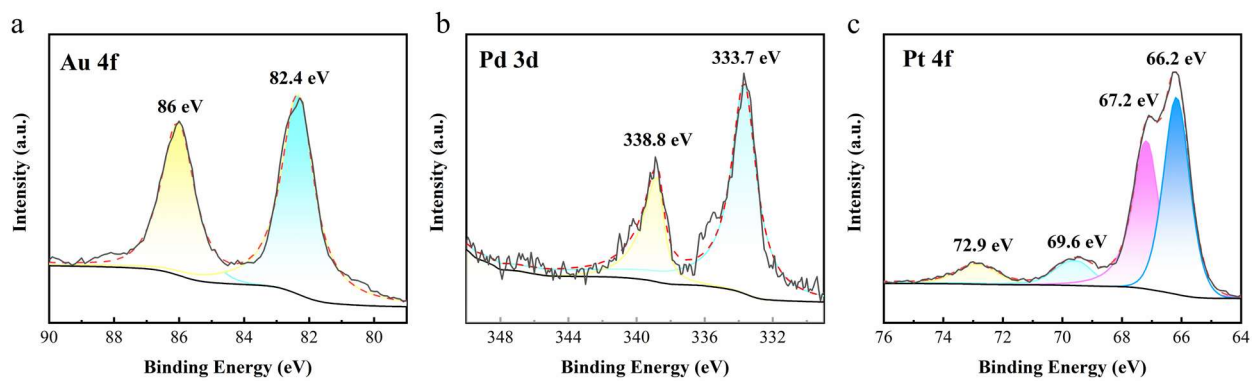


Figure S3. X-ray photoelectron spectroscopy of Au@PdPt (CTAB) trimetallic structure: (a) Au 4f spectrum, (b) Pd 3d spectrum, and (c) Pt 4f spectrum.

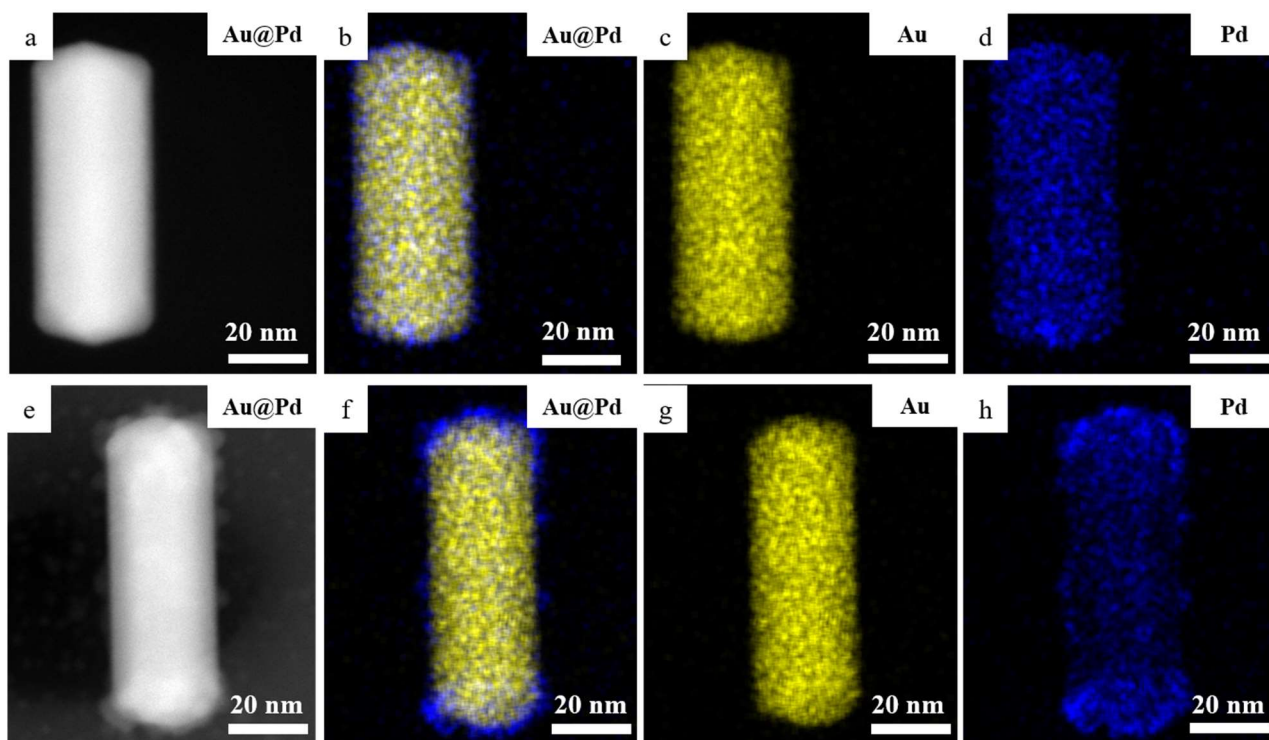


Figure S4. HAADF-STEM images and EDS mapping images of Au@Pd synthesized with different surfactants. (a-d) HAADF-STEM image and EDS mapping images of Au@Pd (CTAB); (e-h) HAADF-STEM image and EDS mapping images of Au@Pd (CTAC). Au is shown in yellow, Pd in blue, and HAADF-STEM in white.

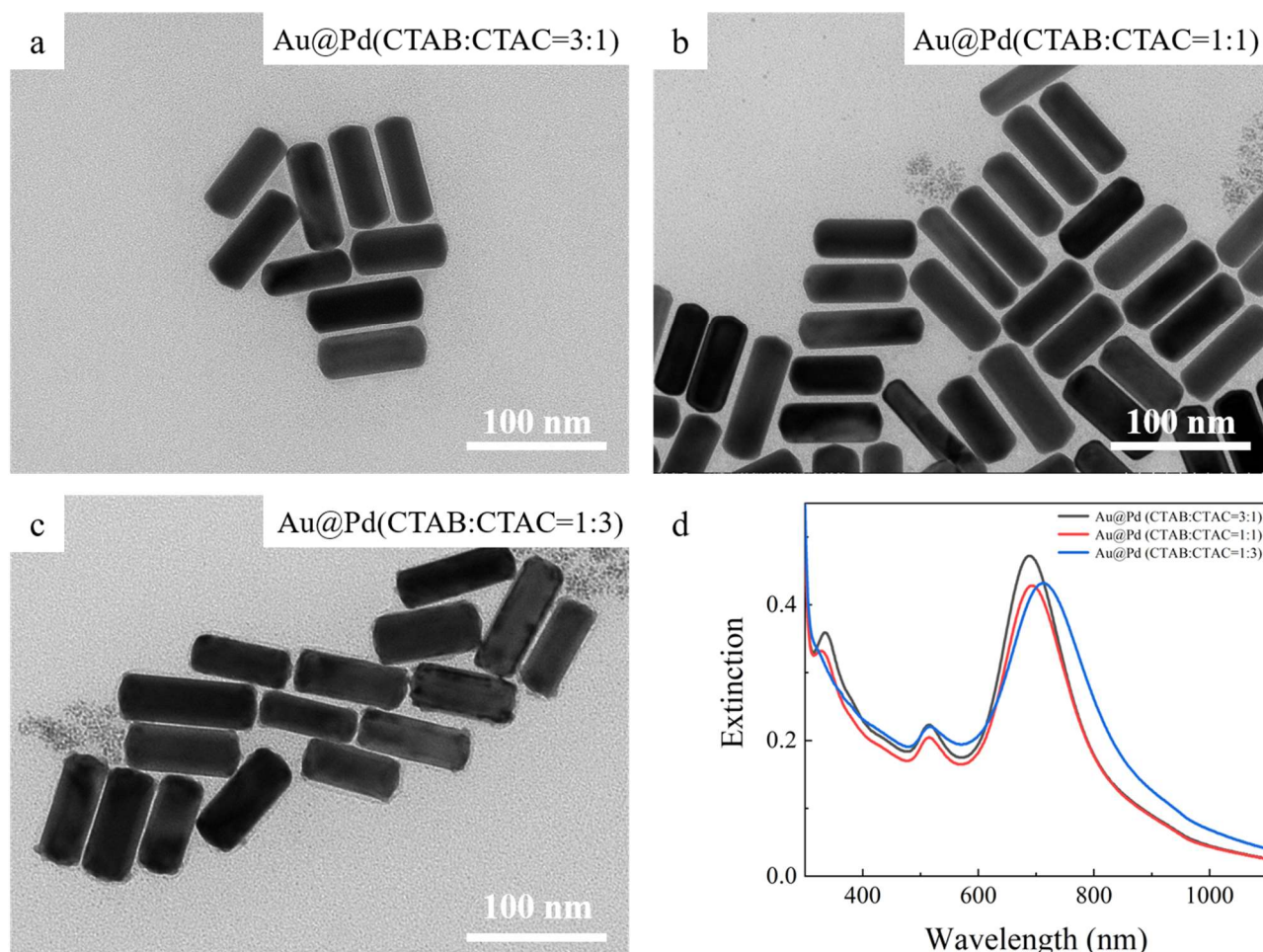


Figure S5. TEM images and UV-Vis spectra of Au@Pd synthesized using mixed surfactants with different CTAB/CTAC ratios. (a-c) TEM images of Au@Pd nanostructures synthesized with CTAB/CTAC ratios of 3:1 (a), 1:1 (b), and 1:3 (c). (d) Corresponding UV-Vis extinction spectra of the samples.

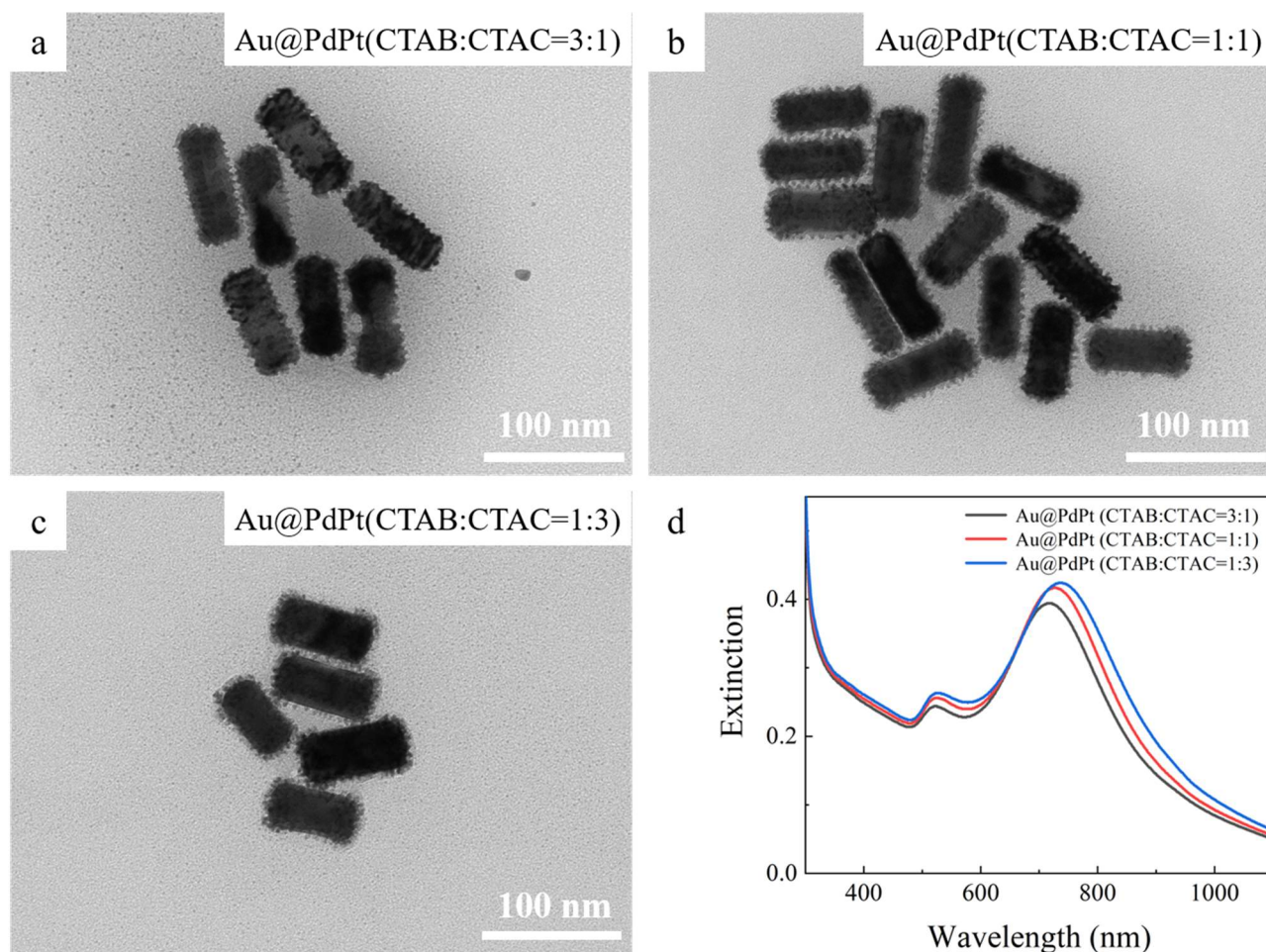


Figure S6. TEM images and UV-Vis spectra of Au@PdPt SSs synthesized using mixed surfactants with different CTAB/CTAC ratios. (a-c) TEM images of Au@PdPt SSs nanostructures synthesized with CTAB/CTAC ratios of 3:1 (a), 1:1 (b), and 1:3 (c). (d) Corresponding UV-Vis extinction spectra of the samples.

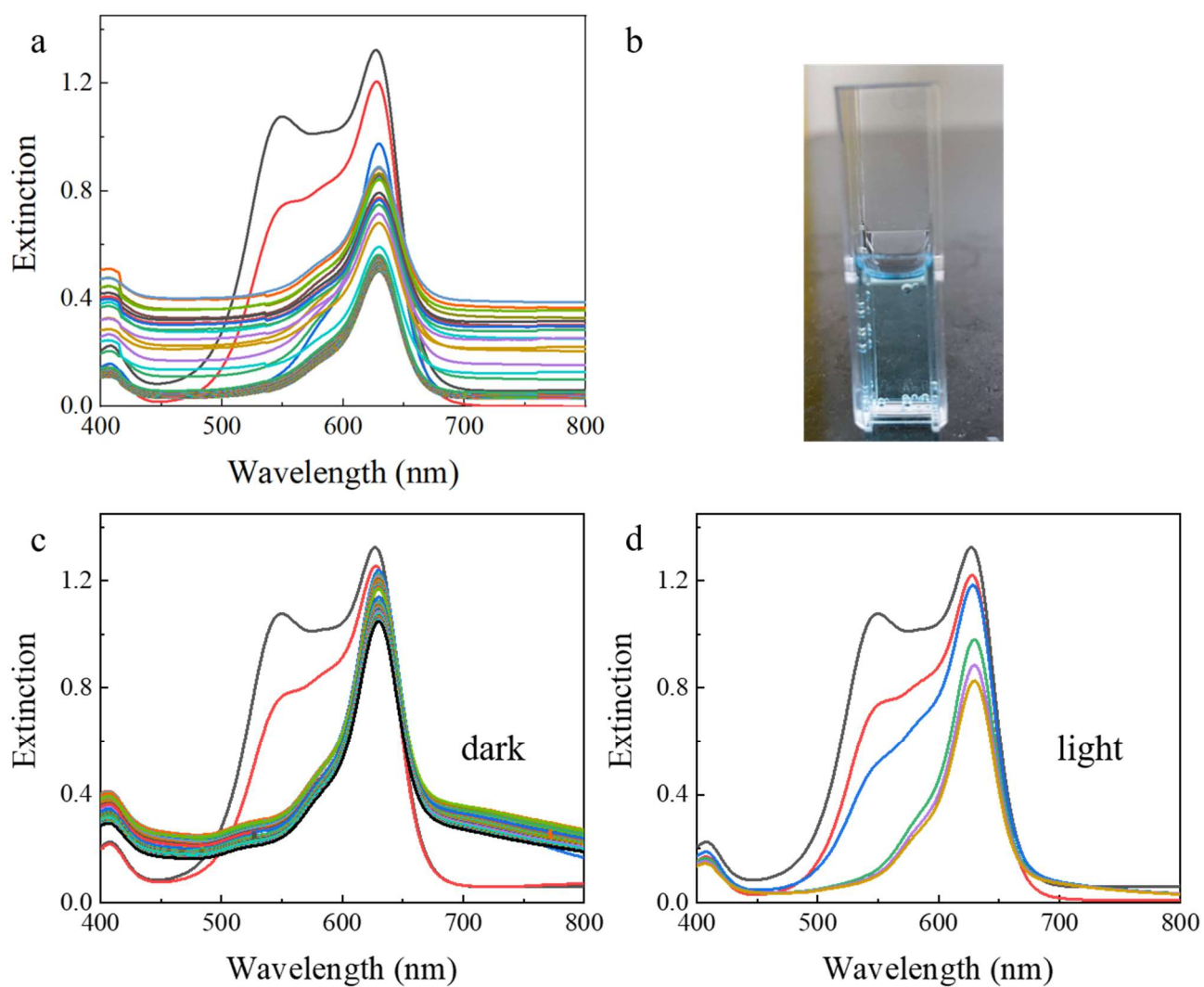


Figure S7. Raw experimental data of MB photocatalytic reactions under different conditions. (a) Raw data of MB reduction by NaBH_4 without a catalyst (no significant difference with or without light, measured every 10 min for 1000 min). (b) Photograph of MB solution after 41 h of reduction. (c) Raw data of MB photocatalysis using AuNRs under dark conditions (measured every 1 min for 55 min). (d) Raw data of MB photocatalysis using AuNRs under light irradiation (measured every 12 min for 48 min).

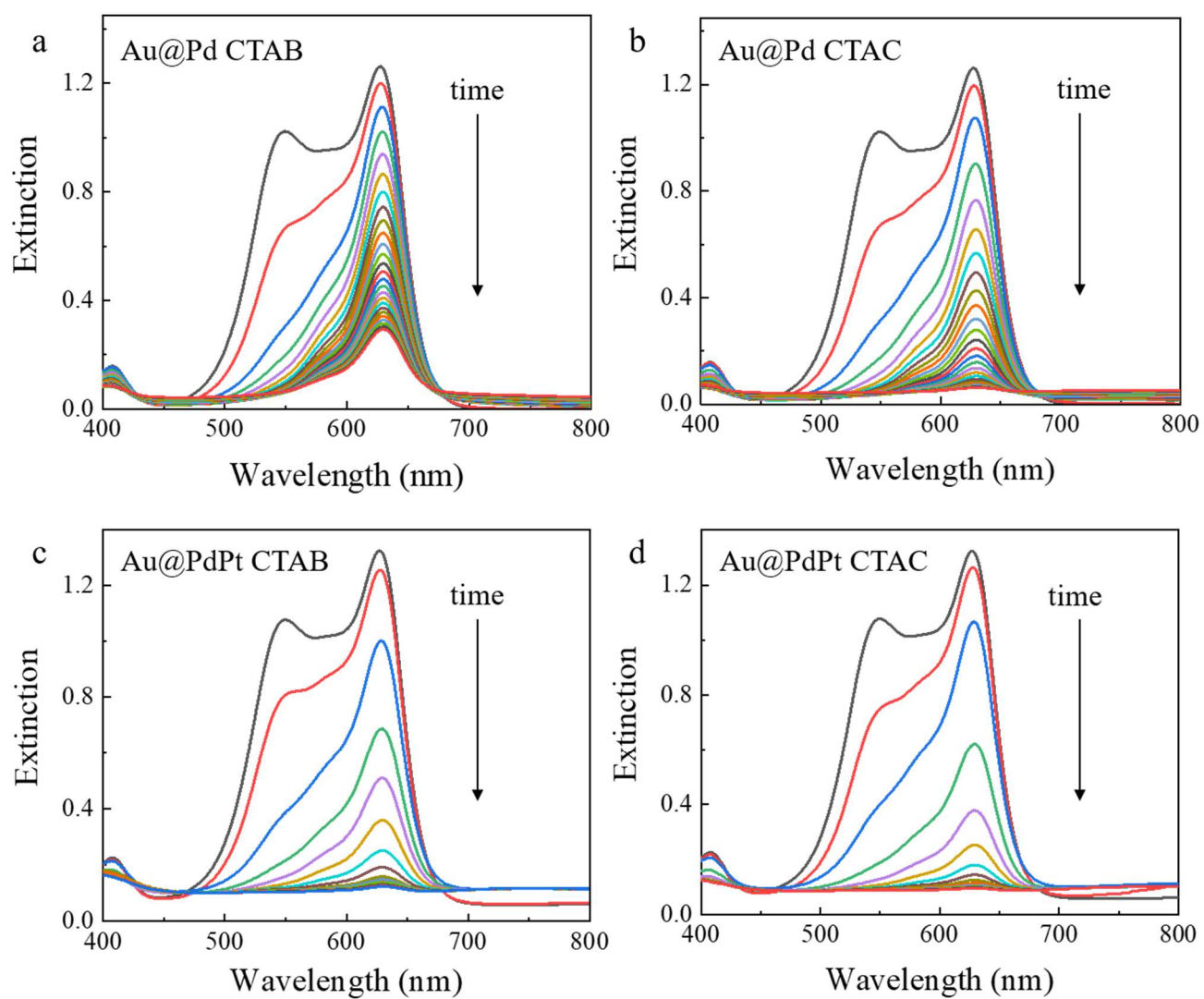


Figure S8. Raw data of MB catalytic reduction by Au@Pd and Au@PdPt SSs under dark conditions. (a) Au@Pd (CTAB), (b) Au@Pd (CTAC), (c) Au@PdPt (CTAB), (d) Au@PdPt (CTAC).

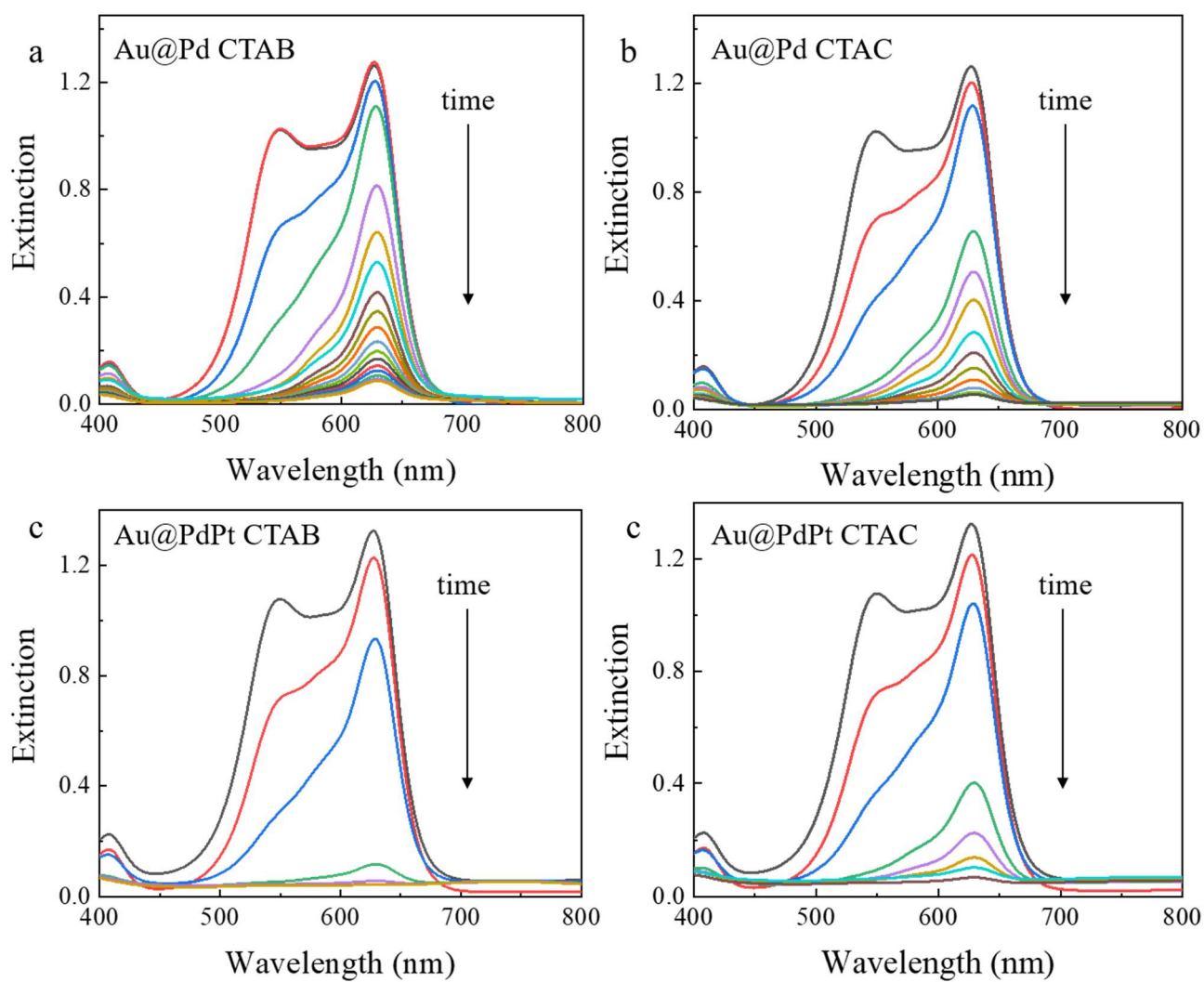


Figure S9. Raw data of MB photocatalytic reduction by Au@Pd and Au@PdPt SSs under visible light irradiation. (a) Au@Pd (CTAB), (b) Au@Pd (CTAC), (c) Au@PdPt (CTAB), (d) Au@PdPt (CTAC).

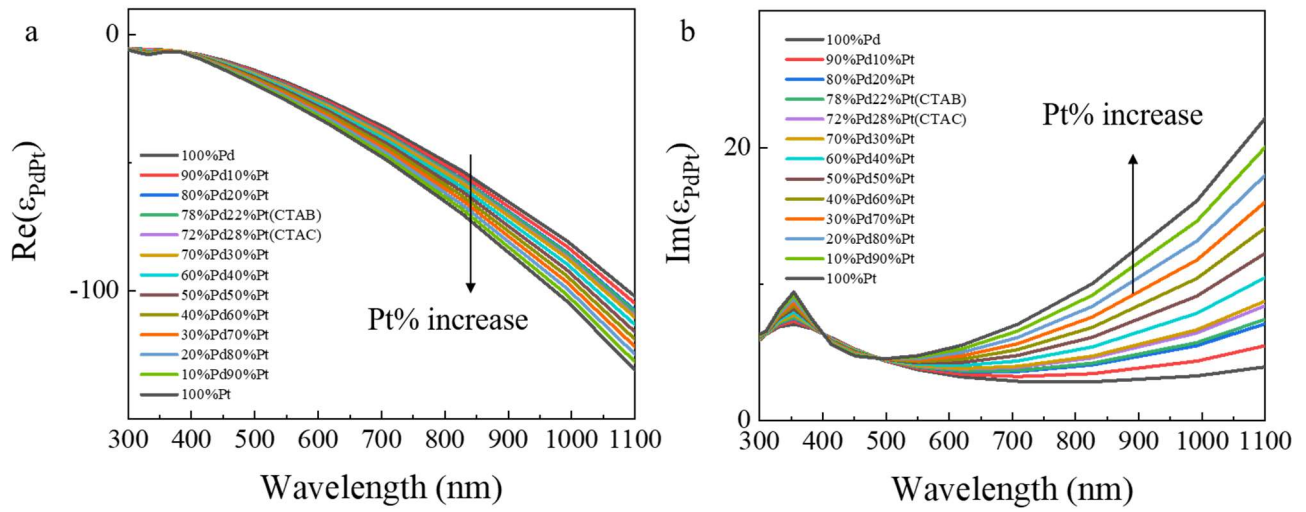


Figure S10. Wavelength-dependent real and imaginary parts of the effective dielectric function of the PdPt alloy, calculated by the Maxwell-Garnett equation for use in FDTD simulations.

Table S1. The fitted rate slopes for methyl blue degradation under dark and light conditions using different nanostructures as catalysts

Samples	Rate (dark)	Rate (light)
Au@Pd (CTAB)	0.06	0.09
Au@Pd (CTAC)	0.14	0.16
Au@PdPt (CTAB)	0.29	0.69
Au@PdPt (CTAC)	0.26	0.28